A comparative study on the distinct regulatory mechanisms of varied nanomaterials in recycled aggregate concrete

Powder Technology 482 (2026) 122731

Contents lists available at ScienceDirect

Powder Technology

journal homepage: www.journals.elsevier.com/powder-technology

A comparative study on the distinct regulatory mechanisms of varied nanomaterials in recycled aggregate concrete

Jing Xu [a,c,1], Peimin Zhan [b,1], Roman Fediuk [d], Dapeng Wang [b], Dongdong Wang [b], Junqing Zuo [e,*], Juan Wang [f,*]

[a] Key Laboratory for Special Area Highway Engineering of Ministry of Education, Chang'an University, South 2nd Ring Road Middle Section, Xi'an, Shaanxi 710064, China
[b] CCCC Shanghai Harbor Engineering Design & Research Institute Co., Ltd, Shanghai 201804, China
[c] Key Laboratory of Advanced Civil Engineering Materials (Ministry of Education), School of Materials Science and Engineering, Tongji University, Shanghai 201804, China
[d] Far Eastern Federal University, 690922 Vladivostok, Russia
[e] Shanghai Construction Group Co., Ltd, Shanghai 200080, China
[f] Department of Architecture and Civil Engineering, Chalmers University of Technology, Gothenburg 41296, Sweden

HIGHLIGHTS

- Comparative study of NCSH, NTO, and NS reveals time-dependent mechanisms governing RAC strength and durability.
- NCSH accelerates early hydration, NTO improves matrix uniformity, and NS promotes later densification.
- Multi-scale microstructural evidence guides targeted nanomaterial selection and synergistic design for RAC.

GRAPHICAL ABSTRACT

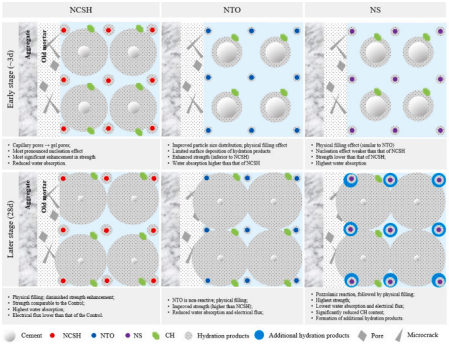

ARTICLE INFO

Keywords:
Recycled aggregate concrete
Nano C-S-H
Nano titanium dioxide
Nano silica
Regulatory mechanisms

ABSTRACT

This study systematically investigates the mechanistic distinctions in how the type of nanomaterials regulates the performance of recycled aggregate concrete (RAC) under comparable particle size conditions. Three nanomaterials-nano calcium silicate hydrate (NCSH), nano titanium dioxide (NTO), and nano silica (NS) were each incorporated at 2 wt% to evaluate their effects on mechanical properties, durability, and microstructural evolution. The results reveal pronounced time-dependent efficacy among the nanomaterials. NCSH exhibited the strongest enhancement in early-age mechanical performance, increasing 1-day compressive and splitting tensile strengths by 56.9% and 41.9%, respectively. In contrast, NS demonstrated superior long-term strength development and permeability resistance, achieving a 20.1% reduction in 28-day water absorption and chloride ion penetration. Microstructural analyses indicate that NCSH primarily accelerates early hydration and structural

* Corresponding authors.
E-mail addresses: Junqingzuo@163.com (J. Zuo), juanw@chalmers.se (J. Wang).
[1] Equal contributions.

https://doi.org/10.1016/j.powtec.2026.122731
Received 8 March 2026; Received in revised form 5 May 2026; Accepted 27 May 2026
Available online 27 May 2026

densification through homogeneous nucleation. NS refines the pore structure and reduces calcium hydroxide content via sustained pozzolanic reactions, while NTO contributes mainly through physical filling and microstructural packing. These findings provide a mechanistic basis for the targeted selection and synergistic optimization of nanomaterials in RAC systems tailored to specific performance requirements.

1. Introduction

With the rapid expansion of the global construction industry, the generation of construction and demolition waste (CDW) has increased dramatically, posing significant environmental and resource-management challenges. The valorization of CDW through the production of recycled aggregate concrete (RAC) has been widely recognized as an effective pathway toward low-carbon transformation and circular resource utilization in the construction sector [1,2]. By partially or fully substituting natural aggregates with recycled coarse aggregates (RCA), the consumption of virgin mineral resources and associated carbon emissions can be substantially reduced [3]. Despite its environmental advantages, RAC generally exhibits inferior mechanical performance and durability compared with conventional concrete. This deterioration is primarily attributed to the intrinsic deficiencies of RCA, including high porosity, pre-existing microcracks, adhered old mortar, and the presence of multiple interfacial transition zones (ITZs) between the aggregate, old mortar, and newly formed cement paste [4]. These structural heterogeneities result in stress concentration, accelerated ingress of aggressive agents, and compromised long-term stability. Therefore, enhancing interfacial compactness and optimizing the overall microstructural integrity of RAC represent critical scientific challenges for achieving high-performance and durable recycled concrete suitable for structural applications.

In recent years, advances in nanotechnology have introduced new opportunities for microstructural regulation of cementitious materials. Owing to their ultra-high specific surface area and elevated surface reactivity, nanomaterials can significantly influence cement hydration kinetics, nucleation processes, and pore structure refinement [5]. Nano silica (NS), for instance, acts both as a nucleation site for C-S-H formation and as a highly reactive pozzolanic agent, thereby accelerating hydration and refining pore structure [6]. Numerous studies have demonstrated that NS can enhance compressive strength, reduce porosity, and improve resistance to chloride ingress in ordinary concrete [7]. In RAC systems, NS has also been reported to refine pore structure and densify the ITZ, thereby improving both mechanical properties and durability [8]. However, the effectiveness of NS is highly dependent on dispersion quality and dosage, and excessive addition may lead to agglomeration and reduced workability [9]. In comparison, nano titanium dioxide (NTO) has been reported to enhance durability through micro-filling effects and, in some cases, photocatalytic functionality that may mitigate surface contamination and degradation [10]. In RAC, NTO has been shown to improve early-age strength and reduce water absorption, although its long-term performance enhancement is often less pronounced than that of NS [11]. The relatively inert nature of NTO suggests that its regulatory effect is primarily physical rather than chemical. Nano C-S-H (NCSH) seeds differs fundamentally from both NS and NTO. As pre-formed C-S-H seeds, NCSH shows strong chemical compatibility with cement hydrates and can markedly accelerate early hydration by lowering the nucleation barrier for C-S-H formation [12]. This effect is especially beneficial for early-age strength development and rapid ITZ densification [13,14]. Recent studies have shown that NCSH can significantly shorten the induction period of cement hydration and promote the formation of a denser microstructure at very early ages [15]. In RAC, NCSH has been reported to improve interfacial bonding and reduce early-age porosity, although its long-term pozzolanic contribution is limited due to the absence of reactive silica [16].

Despite increasing interest in nanomodified RAC, the available evidence remains insufficient to establish a clear mechanistic understanding. Most previous studies have focused either on conventional cement-based materials or on RAC incorporating a single type of nanomaterial [17,18], so the relative effectiveness of different nanomaterials in RAC has not been evaluated within a unified experimental framework. More importantly, the key variables governing nanomodification-particularly particle size, morphology, and chemical nature—have often varied simultaneously among studies. As a result, the respective contributions of chemical reactivity, nucleation, and physical filling remain difficult to distinguish [19,20]. This limitation is especially critical for RAC, whose inherently porous RCA and complex multi-ITZ structure make its microstructural response far more sensitive to nanoscale modification than that of conventional concrete [21,22]. Consequently, the central unresolved issue is not whether nanomaterials can improve RAC, but which mechanism predominates when nanomaterials with different chemistries are introduced under comparable physical conditions. A controlled comparison at similar particle size is therefore essential, because it minimizes size-induced packing differences and allows the role of intrinsic material chemistry to be assessed more directly. Such an approach is needed to determine whether the performance gains arise primarily from pozzolanic reaction [23], C-S-H seeding, or inert filling [24], and thus to establish a clearer framework for interpreting nanomodification pathways in RAC [25]. This is the critical problem that previous studies have not adequately addressed.

Accordingly, this study systematically investigates the modifying effects of NCSH, NTO, and NS on the mechanical performance, water absorption, and chloride ion permeability of RAC under comparable particle size conditions. Thermogravimetric analysis (TG), back-scattered electron imaging (BSE), and nitrogen adsorption-desorption porosity analysis were employed to elucidate the underlying mechanisms governing hydration evolution, pore structure optimization, and interfacial densification. By establishing a direct comparison among NCSH, NTO, and NS, this study addresses a key gap in current research and provides a mechanistic basis for the rational selection of nanomaterials in high-performance recycled aggregate concrete.

2. Materials and experimental program

2.1. Raw materials

P. I 42.5 ordinary Portland cement was employed as the primary binder. RCA were obtained from demolished concrete structures and processed through crushing and sieving. Two particle size fractions (5–10 mm and 10–20 mm) were selected for use. Natural river sand with a fineness modulus of 2.62 (classified as medium sand) served as the fine aggregate. The fundamental physical properties of the aggregates are summarized in Table 1. NS was supplied by Shandong Taipeng New Materials Co., Ltd., and NTO was provided by Suzhou Carbon Feng

Table 1
Physical properties of aggregates.

Type	Water absorption (%)	Apparent density (kg/m^3)	Bulk density (kg/m^3)	Crushing index (%)
Natural fine aggregate	/	2612	1630	/
RCA (5–10 mm)	6.1	2512	1373	/
RCA (10–20 mm)	4.1	2489	1424	16.2

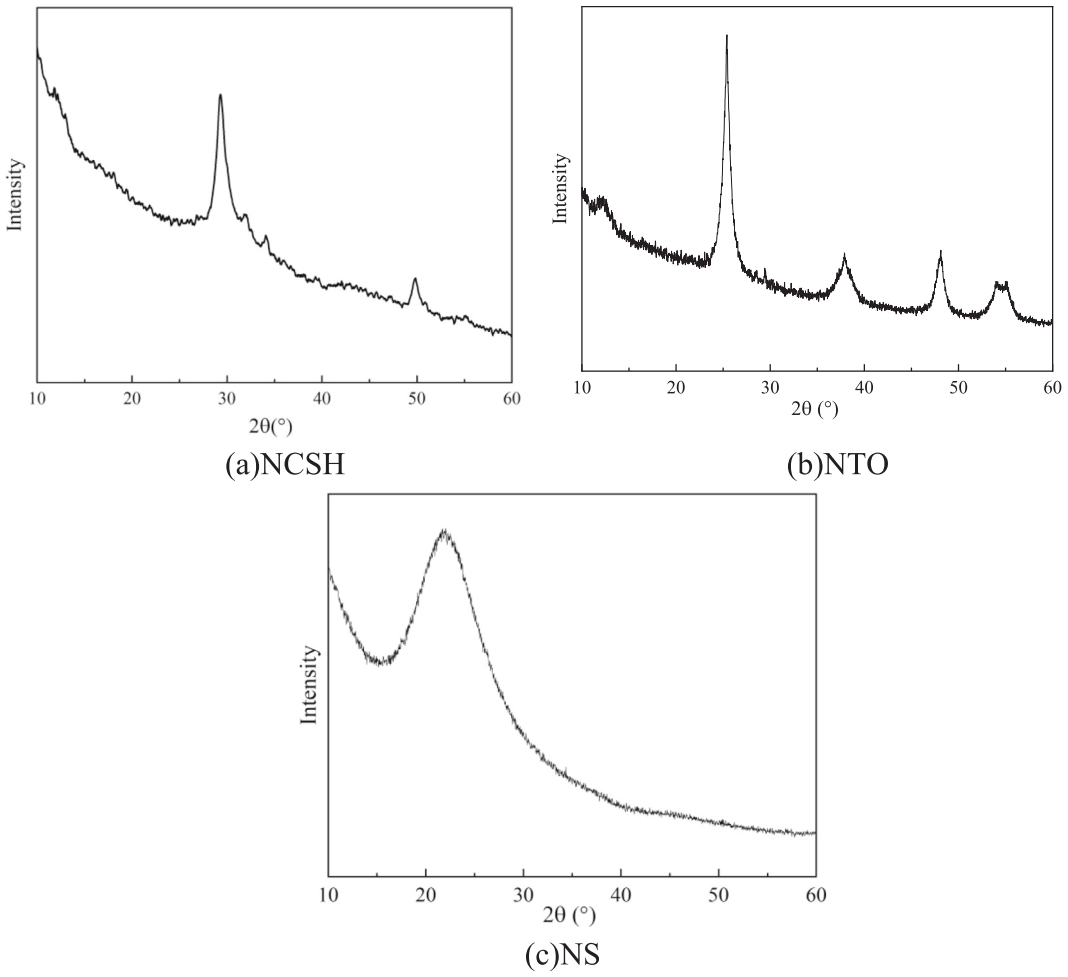

Fig. 1. XRD pattern of different nanomaterials.

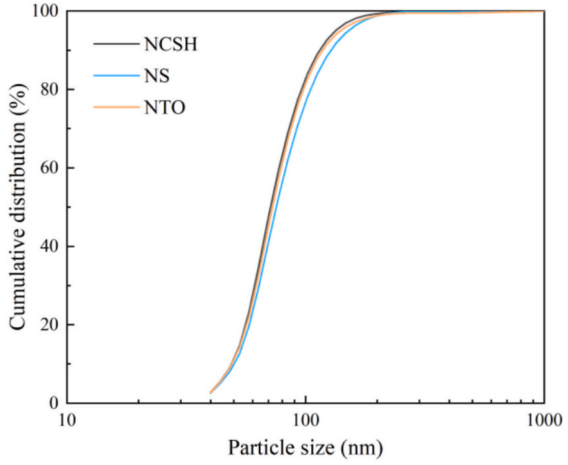

Fig. 2. Particle size distribution curves of different nanomaterials.

Graphene Technology Co., Ltd. NCSH was synthesized via a hydrothermal method; the detailed synthesis protocol has been described elsewhere [26].

Fig. 1 presents the microstructural characterization of the synthesized NCSH. X-ray diffraction (XRD) patterns exhibit characteristic diffraction peaks at 2θ ≈ 29.2°, 32.3°, and 49.7°, corresponding to calcium silicate hydrate phases, while no discernible portlandite (CH) peaks were detected, confirming that C-S-H constitutes the primary hydration product in the synthesized material [27]. For NTO, distinct diffraction peaks located at 2θ ≈ 25.3°, 37.8°, 48.0°, and 54.0° can be assigned to the anatase phase of TiO_2, confirming its high crystallinity. NS, the XRD pattern shows a broad diffuse hump in the range of 2θ ≈ 20–25°, characteristic of its predominantly amorphous silica structure. Particle size distributions of NCSH, NTO, and NS were determined using a laser particle size analyzer (LS230). As illustrated in Fig. 2, all three nanomaterials exhibited comparable size distributions, with average particle diameters ranging from 90 to 95 nm and median diameters between 80 and 85 nm. The relatively concentrated distributions ensure the validity of comparative analysis by minimizing particle size–related variability, thereby allowing mechanistic differences arising from chemical composition to be isolated. The purities of NCSH, NTO, and NS were approximately 80%, 99.0%, and 99.5%, respectively. Their BET specific surface areas were 77.5, 84.2, and 112.4 m^2/g, respectively.

2.2. Mixture proportions

To systematically compare the effects of representative nanomaterials (NCSH, NTO, and NS) on the mechanical performance, durability, and microstructural characteristics of RAC, four mixture groups were designed. A control mixture without nanomaterials (RAC0) was used as the reference. All nanomaterials were incorporated via direct external addition at a dosage of 2 wt% relative to cement mass. The water-to-cement ratio (w/c) of RAC was fixed at 0.35, and the sand ratio was maintained at 40%. Considering the elevated water absorption capacity of RCA, an additional 37.5 kg/m^3 of mixing water was introduced to compensate for internal absorption. A polycarboxylate ether (PCE)

Table 2
Mix design of RAC modified by addition of nanomaterials (kg/m^3).

Samples	Cement	Water	Nanomaterials			Sand	RCA		Additional water	PCE
			NCSH	NTO	NS		5–10 mm	10–25 mm		
RAC0	450	157.5	0	/	/	713	428	642	37.5	2.2
RAC-2.0CSH	450	157.5	9	/	/	713	428	642	37.5	3.2
RAC-2.0NTO	450	157.5	/	9	/	713	428	642	37.5	2.9
RAC-2.0NS	450	157.5	/	/	9	713	428	642	37.5	3.8

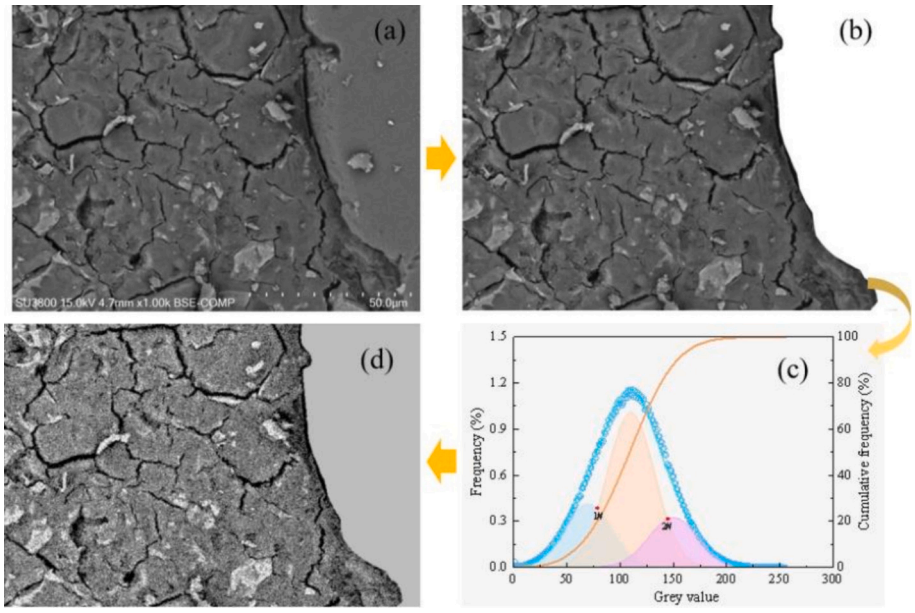

Fig. 3. (a) BSE images, (b) BSE images after aggregate removal, (c) critical points of pores, hydration products, and unhydrated phases in the ITZ obtained via Gaussian fitting, and (d) processed BSE images.

was used to adjust workability, with the dosage tailored to maintain a slump range of 180–220 mm to ensure consistency across mixtures. The variation in PCE demand is mainly attributed to differences in the specific surface area, dispersion characteristics, and water adsorption capacity of the nanomaterials. In particular, NS required a higher PCE dosage due to its finer particle size and stronger tendency to agglomerate, whereas NCSH and NTO exhibited relatively lower PCE demand. Detailed mixture proportions are presented in Table 2.

After casting, specimens were demolded after 24 h at room temperature and subsequently cured in a standard curing chamber (20 ± 2 °C, relative humidity ≥95%) until the designated testing ages. In parallel, cement paste samples with identical binder compositions were prepared for microstructural characterization. Sample designations follow the format "C-2.0CSH," indicating cement paste incorporating 2 wt% NCSH.

2.3. Test methods

2.3.1. Mechanical properties

Compressive and splitting tensile strength tests were carried out in accordance with GB/T 50081–2019. Cube specimens with dimensions of 100 × 100 × 100 mm were used, with loading rates of 0.5 MPa/s for compressive strength and 0.06 MPa/s for splitting tensile strength, respectively. For each mixture, three specimens were tested, and the arithmetic mean was reported.

2.3.2. Water absorption

Water absorption was measured following ASTM C1585–13 using a gravimetric method. Cubic specimens (100 mm × 100 mm × 100 mm) were monitored at specified time intervals up to 72 h. The evolution of water absorption with time was calculated to evaluate capillary transport behavior.

2.3.3. Chloride ion penetration

Rapid chloride permeability tests (RCPT) were performed in accordance with ASTM C1202. Cylindrical specimens (Φ100 mm × 300 mm) were tested at 28 days. A 0.3 mol/L NaOH solution was used as the anolyte, while a 3 wt% NaCl solution served as the catholyte. The total charge passed (Coulombs) was recorded to assess resistance to chloride ion penetration.

2.3.4. BSE imaging

BSE images of cement paste matrices and RAC ITZs were obtained using a scanning electron microscope (Zeiss EVO LS15) under the following conditions: accelerating voltage 15 kV, working distance 10 mm, and magnification 1000×. Prior to imaging, specimens were cut into small sections (~10 mm × 10 mm × 5 mm), vacuum-impregnated with low-viscosity epoxy to preserve pore structure, and subsequently ground using SiC papers of progressively finer grit sizes (from 400 to 8000 grit). Subsequently, the samples were polished with 1 μm and 0.3 μm alumina polishing liquid to achieve a smooth, scratch-free surface suitable for BSE imaging. The polished samples were then coated with a thin conductive carbon layer to minimize charging effects. As shown in Fig. 3(a), representative ITZ regions were selected. Aggregate particles were digitally removed using image editing software to isolate the matrix region (Fig. 3b). Image segmentation and quantitative phase analysis were conducted using Image-Pro software combined with Gaussian distribution fitting to distinguish pores/microcracks, hydration products, and unhydrated cement particles (Fig. 3c). In the processed images (Fig. 3d), pores and microcracks appear black, hydration products dark

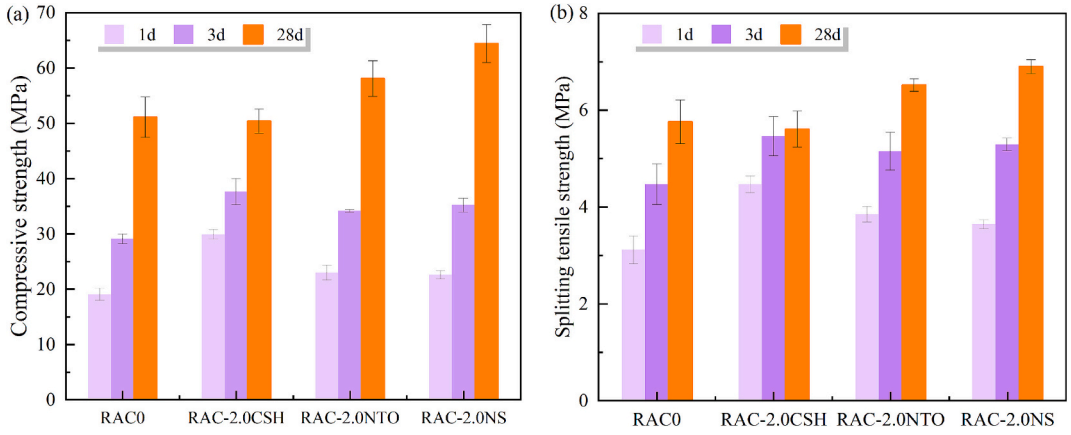

Fig. 4. Mechanical properties of RAC: (a) compressive strength and (b) splitting tensile strength.

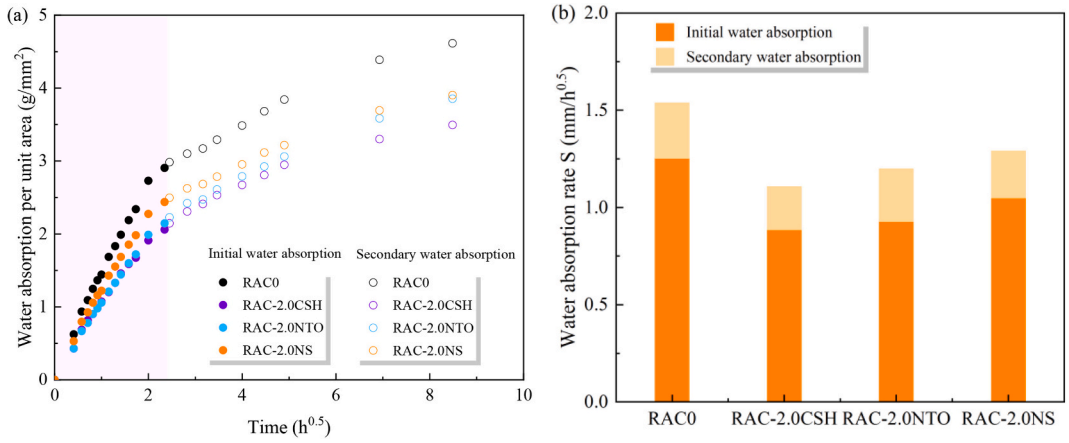

Fig. 5. Water absorption of RAC samples at 1 day: (a) water absorption per unit area and (b) water absorption rates of different samples.

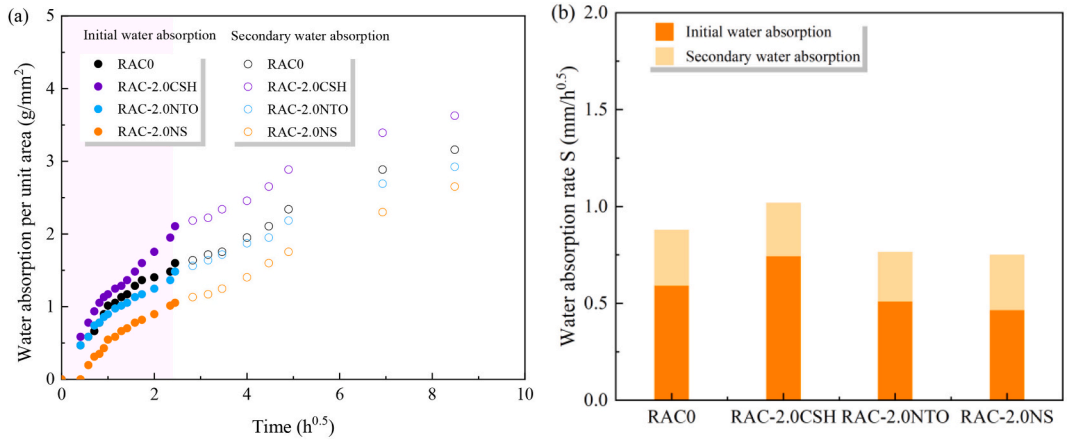

Fig. 6. Water absorption of RAC samples at 28 days: (a) water absorption per unit area and (b) water absorption rates of different samples.

gray, unhydrated particles white, and RCA light gray. Detailed image analysis procedures are described in Refs. [14, 28]. It should be noted that microcracks may be locally introduced during grinding and polishing; however, epoxy impregnation and careful surface preparation were employed to minimize such artifacts, and their potential influence on quantitative analysis is considered limited.

For each mixture, at least 3 representative ITZ regions from different locations were analyzed to ensure statistical reliability. All reported phase fractions were obtained as mean values, and the corresponding standard deviations were calculated to account for spatial variability.

2.3.5. *TG analysis*

TG analysis was performed using a TA Instruments TGA under nitrogen atmosphere. Samples were heated from 30 °C to 1000 °C at a rate of 10 °C/min. Bound water content (CBW) and portlandite (CH) content were quantified based on mass losses within corresponding temperature intervals.

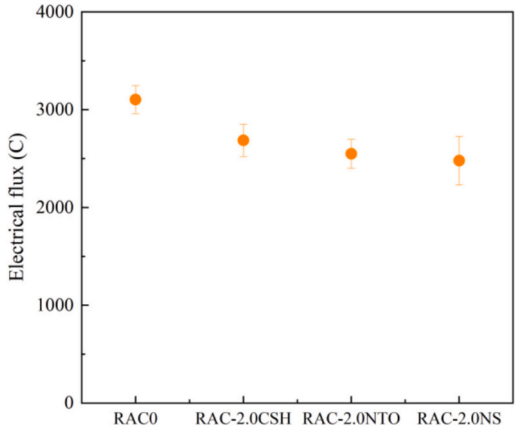

Fig. 7. Electric flux of RAC samples at 28 days.

2.3.6. *Nitrogen adsorption test*

Nitrogen adsorption–desorption measurements were conducted according to ASTM D4222–20 using an Autosorb-iQ3 surface area and porosity analyzer. Cement paste samples cured for 12 h and 72 h were tested to capture early-age pore evolution. Prior to testing, specimens were vacuum-degassed at 200 °C for 2 h to remove physically adsorbed moisture. The pore size distribution in the 1–200 nm range was derived from the adsorption branch of the isotherms using the Barrett-Joyner-Halenda (BJH) method, enabling evaluation of the influence of nanomaterials on early-age pore structure development.

3. Results

3.1. *Mechanical properties*

Fig. 4 presents the evolution of compressive strength and splitting tensile strength of RAC at different curing ages. Overall, all three types of nanomaterials promoted early-age strength development to varying degrees. Among them, the NCSH-incorporated specimens exhibited the most pronounced enhancement in early strength, whereas the NS-incorporated specimens showed more significant strength gains at later ages. Compared with the control group, the 1-day compressive strengths of the RAC specimens containing NCSH and NS increased by 56.9% and 18.7%, respectively; at 28 days, the compressive strength of the NCSH specimen was comparable to the control, whereas that of the NS specimen increased by 23.6%. The early-age effect of NCSH is mainly attributed to its nucleation function, which shortens the induction period and promotes rapid formation of C-S-H gel. By contrast, the later-age benefit of NS arises from its pozzolanic reaction. Active SiO_2 continuously consumes CH and generates secondary C-S-H, leading to

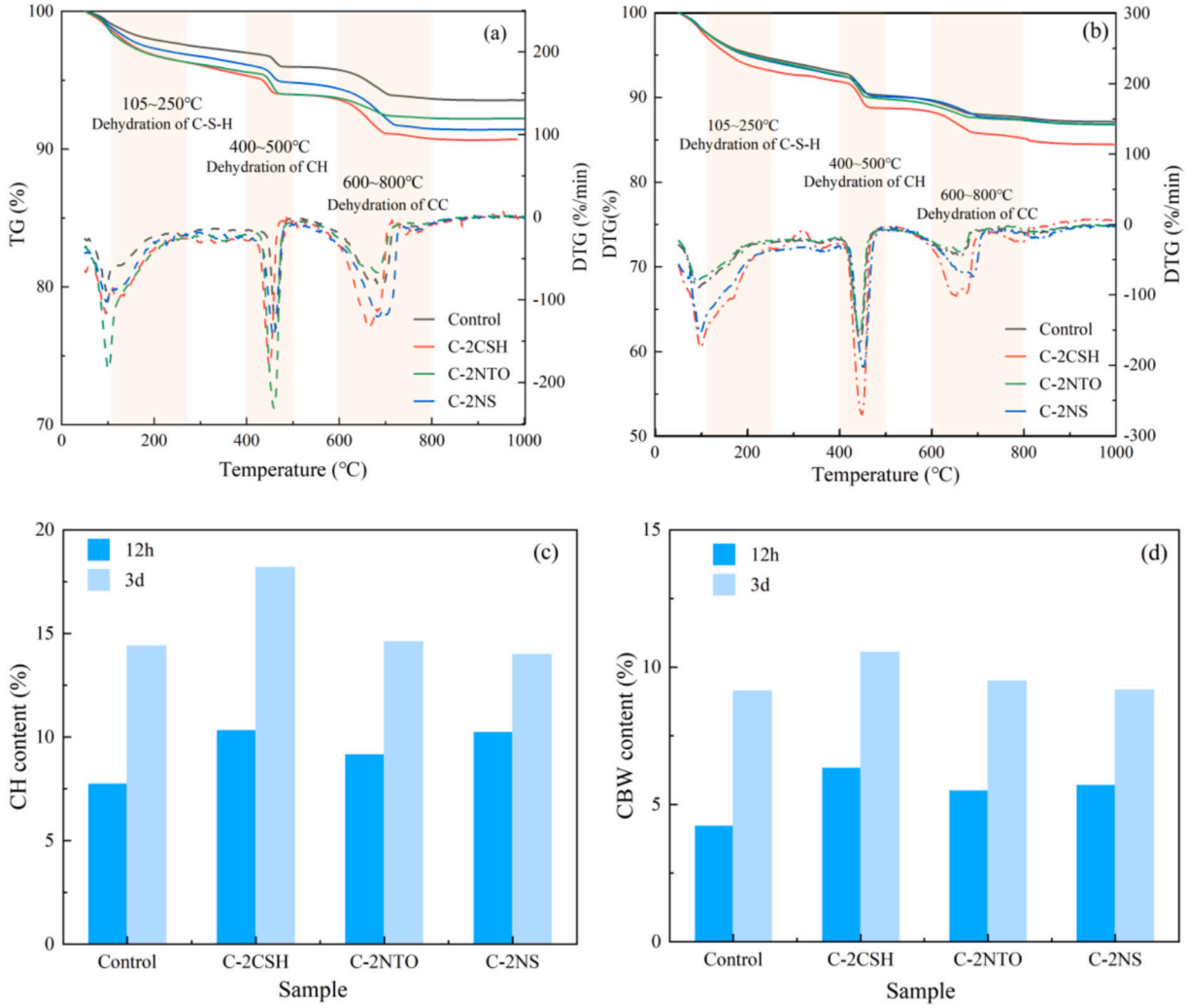

Fig. 8. TG/DTG curves and relative phase content of cement paste: (a) TG/DTG of 12 h specimens, (b) TG/DTG of 3 d specimens, (c) relative CH content, and (d) relative CBW content.

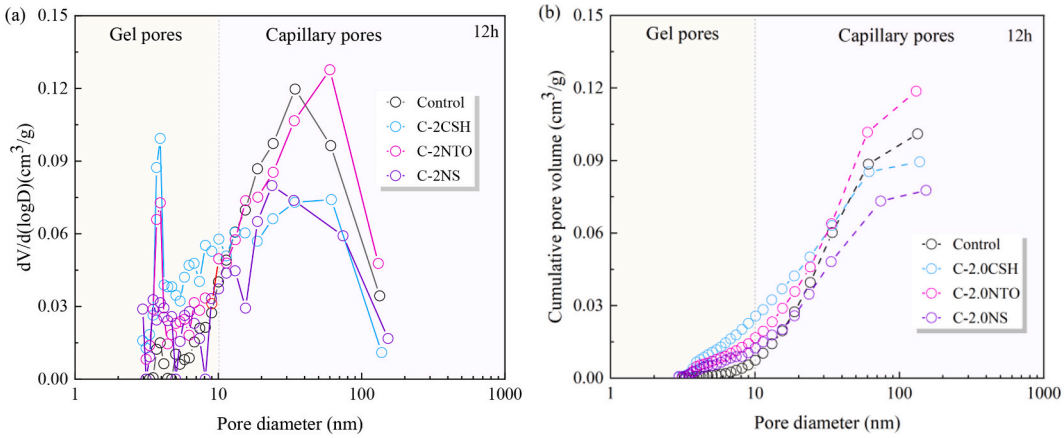

Fig. 9. Pore structure of cement paste at 12 h: (a) pore size distribution, (b) cumulative pore volume.

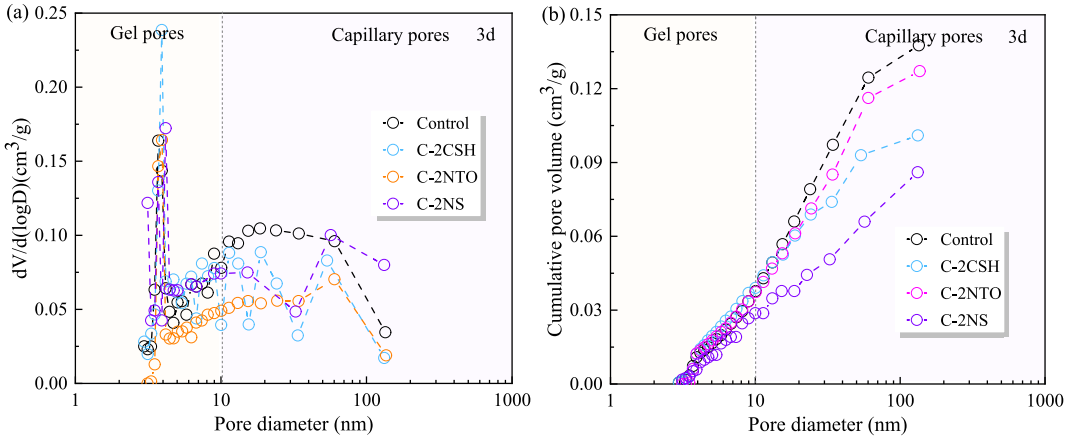

Fig. 10. Pore structure of cement paste at 3 d: (a) pore size distribution, (b) cumulative pore volume.

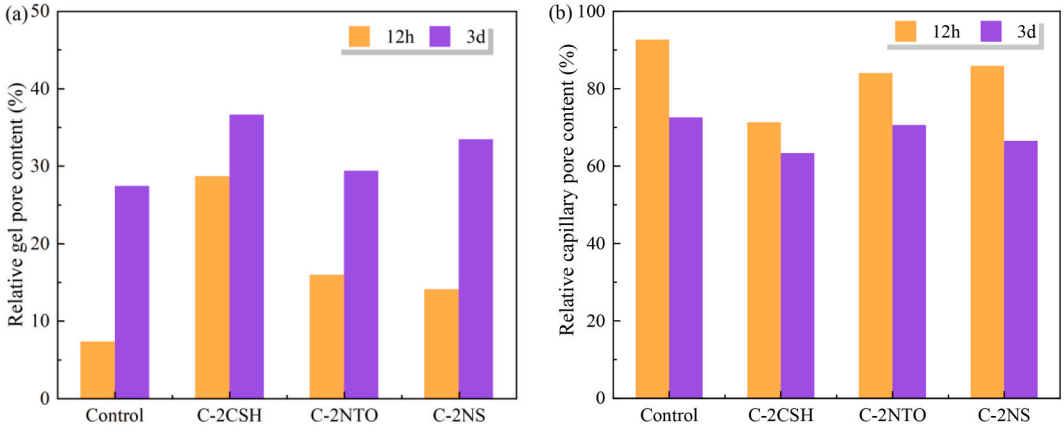

Fig. 11. Pore distribution at 12 h and 3 d: (a) gel pores, (b) capillary pores.

Table 3
Most probable pore diameter and cumulative pore volume of cement pastes.

Sample	Most Probable Pore Diameter (nm)		Pore Volume (cm^3/g)	
	12 h	3d	12 h	3d
Control	34.3	3.7	0.10	0.14
C-2CSH	4	3.9	0.09	0.10
C-2NTO	23	4.1	0.08	0.09
C-2NS	60.1	3.9	0.12	0.13

progressive microstructural refinement and higher load-bearing capacity.

As shown in Fig. 4(b), the evolution of splitting tensile strength follows a trend similar to that of compressive strength. At 1 day, the tensile strengths of RAC specimens containing NCSH, NTO, and NS increased by 41.9%, 22.5%, and 17.4% relative to the control, respectively. However, with increasing curing age, the enhancement effect of NTO gradually diminished, whereas that of NS continued to increase, reaching approximately 19.8%. This behavior indicates that NTO primarily

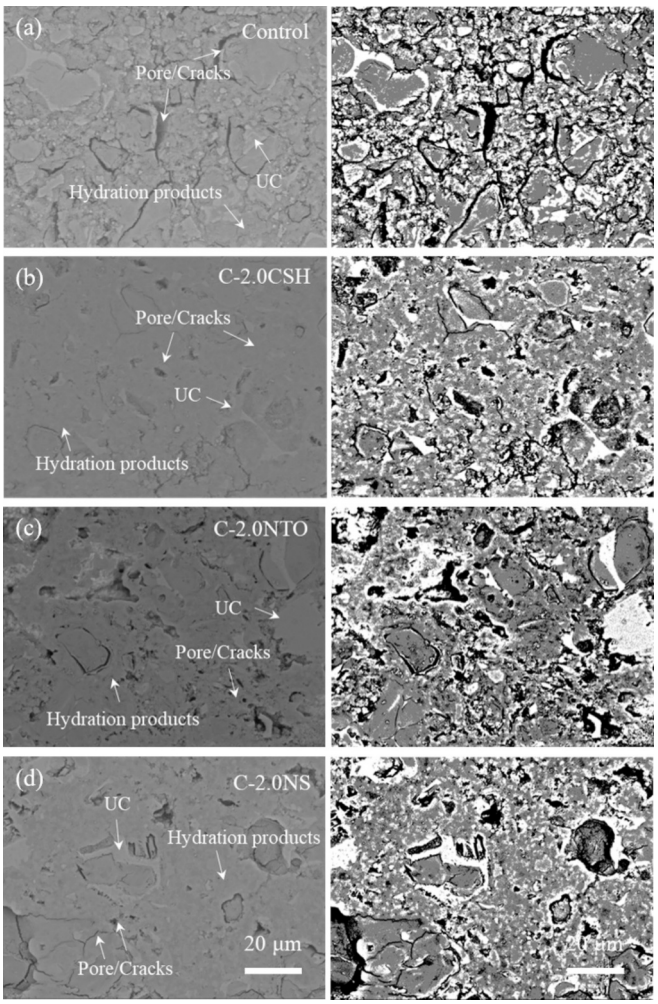

Fig. 12. BSE images of cement paste at 12 h: (a) Control, (b) C-2CSH, (c) C-2NTO, and (d) C-2NS.

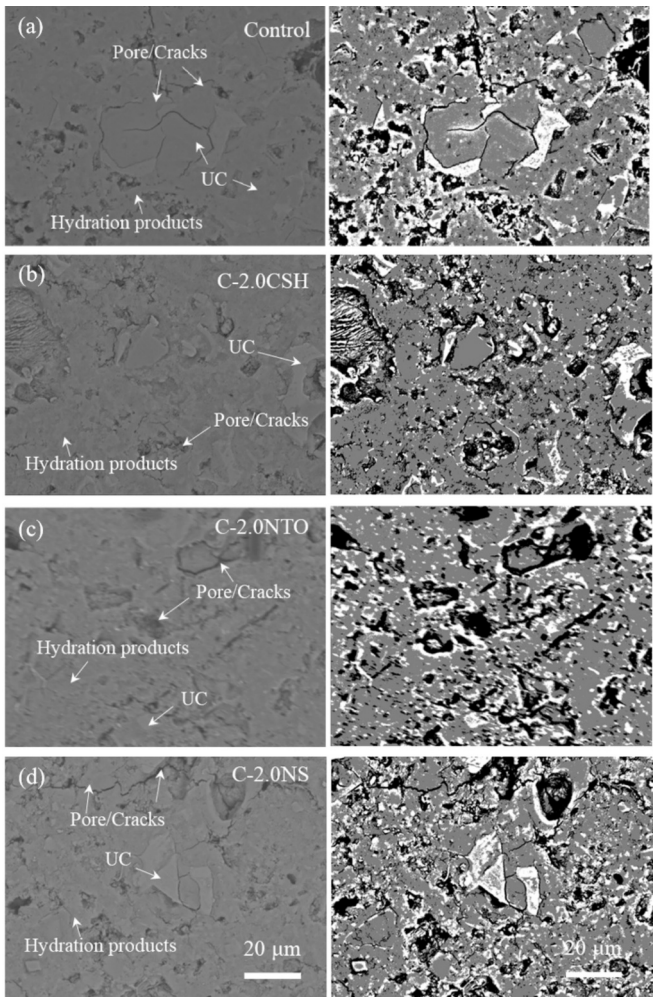

Fig. 13. BSE images of cement paste at 3 d: (a)Control, (b)C-2CSH, (c)C-2NTO and (d)C-2NS.

improves early structural integrity through heterogeneous nucleation and micro-filling effects, while NS enhances the long-term densification of the paste–aggregate interface and pore structure via pozzolanic reactions. Therefore, the mechanisms by which different nanomaterials contribute to strength development exhibit distinct age-dependent characteristics.

3.2. Water absorption

Fig. 5 presents the relationship between cumulative water absorption per unit area and the square root of time within the first 1d for the RAC specimens. All mixtures exhibit a characteristic two-stage absorption behavior. The initial stage is dominated by rapid capillary suction through relatively large pores and pre-existing microcracks, while the subsequent stage corresponds to a slower absorption regime governed primarily by capillary surface tension and progressively reduced hydraulic connectivity within finer pore networks. According to previous studies [29,30], the slope of the linear relationship between water absorption and the square root of time can be defined as the sorptivity coefficient, S, which quantitatively characterizes the capillary water transport capacity of concrete. The sorptivity is calculated as:.

$$S = \frac{\Delta m_s}{\sqrt{t}\rho_w A} \tag{1}$$

where Δm_s denotes the cumulative mass of absorbed water, ρ_w is the density of water (10^{-3} g/mm^3), A represents the cross-sectional area of the specimen in contact with water (mm^2), and t is the elapsed time. As shown in Fig. 5, the incorporation of nanomaterials significantly reduced the water absorption rate of the specimens. At 1d, the RAC specimen containing 2.0% NCSH exhibited a 24.3% lower water uptake compared to the control group. This effect is primarily attributed to the nucleation-promoting action of NCSH, which accelerates the formation of early hydration products, thereby reducing capillary pore connectivity and suppressing capillary water migration. RAC specimens containing NTO and NS also showed lower water absorption than the control. However, their values were higher than that of the 2.0% NCSH specimen, indicating that NCSH was more effective in densifying the microstructure at early age.

For fitting analysis, 6 h was selected as the demarcation point, and all fitting results yielded R^2 values greater than 0.95. The results indicate that the addition of 2.0% NCSH reduced the initial and secondary water absorption rates of RAC by 29.3% and 22.5%, respectively. In contrast, the initial water absorption rates of specimens containing 2.0% NTO and NS decreased by 26.0% and 16.3%, while the secondary water absorption rates decreased by 5.0% and 15.4%, respectively. Notably, the lower secondary water absorption rates observed in the NCSH and NS specimens suggest their more pronounced effectiveness in mitigating microcrack formation and improving pore connectivity.

Fig. 6 presents the water absorption results of RAC specimens at 28 days. With increasing curing age, the water absorption of all specimens decreased significantly. However, unlike the early-age results, a higher

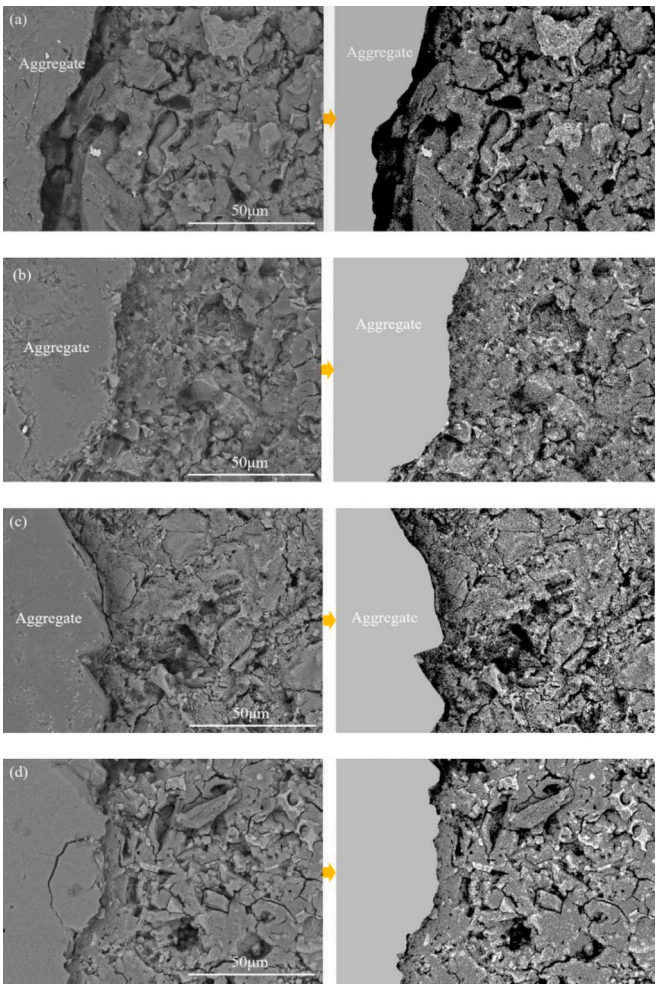

Fig. 14. Microstructure and segmented BSE images of the ITZ in RAC samples at 3 days: (a) RAC0, (b) RAC-2.0CSH, (c) RAC-2.0NTO, and (d) RAC-2.0NS.

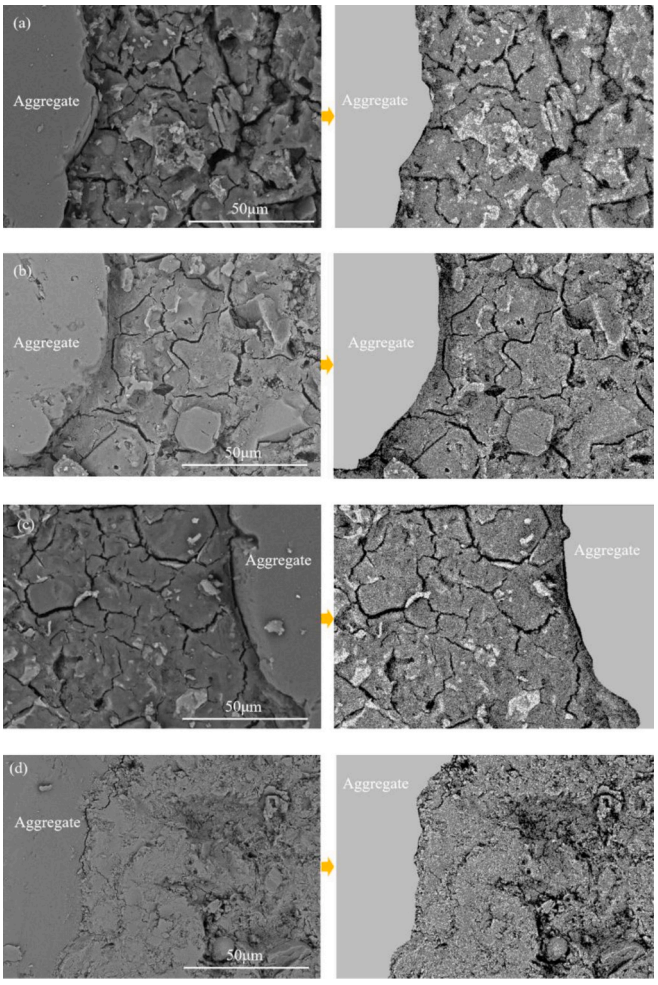

Fig. 15. Microstructure and segmented BSE images of the ITZ in RAC samples at 28 days: (a) RAC0, (b) RAC-2.0CSH, (c) RAC-2.0NTO, and (d) RAC-2.0NS.

NCSH content slightly increased the water absorption per unit area at 28 days. This may be related to the formation of relatively low-density C-S-H at early age, which partially hinders later hydration. In contrast, the NS-containing specimens exhibited the lowest water absorption at 28 days, indicating that the ongoing pozzolanic reaction effectively optimized the pore structure and enhanced long-term impermeability. Overall, NCSH, NTO, and NS all reduced the water absorption of RAC at different stages, with NS demonstrating superior potential for comprehensive durability improvement.

3.3. Chloride ion permeability

Fig. 7 presents the chloride ion charge passed of RAC specimens at 28 days. The measured charge passed for all specimens ranged from 2000 to 3200C, corresponding to a moderate permeability classification. Incorporation of NCSH, NTO, and NS reduced the charge passed by 13.4%, 17.8%, and 20.1%, respectively. Although NCSH was highly effective in refining the early pore structure, NS showed the best overall resistance to ion transport at later age. This result is attributed to its sustained pozzolanic reaction, which further reduces pore connectivity.

3.4. Phase analysis

Fig. 8 presents the TG/DTG curves of the cement paste at 12 h and 3 days. In the DTG curves, three characteristic peaks can be identified. The peak near 105 °C is assigned to the dehydration of C-S-H and other hydration products [31]. The peak between 400 and 500 °C corresponds to the decomposition of CH. The peak between 600 and 800 °C is attributed to the decomposition of carbonates or calcite (CC) [32]. Since the calcium carbonate in the cement paste primarily originates from the carbonation of CH [14], the relative mass fractions of CH and CBW were calculated using the following equations:.

$$\mathrm{mCH_{Total}\%} = \left[(\mathrm{M400} - \mathrm{M500}) \times \frac{74}{18} + (\mathrm{M600} - \mathrm{M800}) \times \frac{74}{44}\right] \times 100\% \tag{2}$$

$$m\mathrm{CBW\%} = \left[(M105 - M600) + (M600 - M800) \times \frac{18}{44}\right] \times 100\% \tag{3}$$

where $M105$, $M400$, $M500$, $M600$ and $M800$ represent the percentage mass loss of the cement paste at 105 °C, 400 °C, 500 °C, 600 °C, and 800 °C, respectively. As shown in Fig. 8c and d, with increasing curing age, the relative contents of CH and CBW increased for all specimens. Among them, the C-2CSH sample consistently exhibited the highest CH and CBW contents at all ages, indicating that NCSH significantly accelerates cement hydration and promotes the formation of additional hydration products [26]. Notably, at 72 h, the CH content of the C-2NTO sample was comparable to that of the control, whereas the CH content of the C-2NS sample was slightly lower than the control. This suggests that NS partially consumed CH through pozzolanic reactions, thereby enhancing later-stage matrix densification and stabilizing the hydration products.

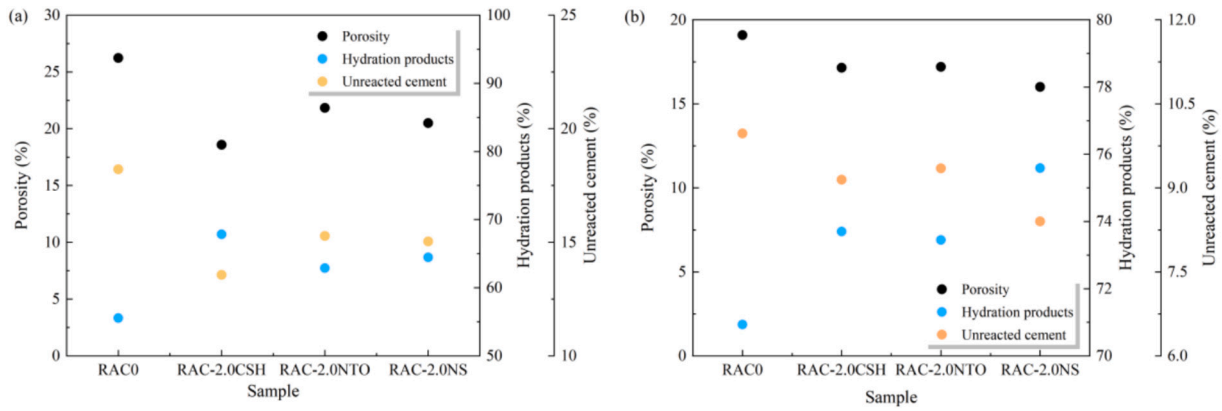

Fig. 16. Relative proportions of pores, hydration products, and unhydrated phases in the ITZ of RAC samples at (a) 3 days and (b) 28 days.

3.5. Pore structure

Figs. 9–11 present the nitrogen adsorption results of cement pastes at different ages, with the most probable pore diameter and total pore volume summarized in Table 3. At 12 h, the cumulative pore volume of the samples ranged from 0.07 to 0.12 cm^3/g, while at 3 days it increased slightly to 0.08–0.14 cm^3/g. This modest increase may be related to the detection limit of nitrogen adsorption, which mainly captures pores smaller than 200 nm. As hydration proceeds, the number of gel pores increases, whereas larger pores are not fully reflected by this method.

At 12 h, the incorporation of NCSH significantly refined the pore structure, reducing both the most probable pore diameter and the total pore volume of the cement paste. Specifically, for the C-2CSH sample, the most probable pore diameter decreased from 34.3 nm to 4 nm, and the total pore volume decreased from 0.10 cm^3/g to approximately 0.09 cm^3/g. The addition of NTO similarly reduced pore size and volume by 32.9% and 20%, respectively. In contrast, NS slightly increased both the most probable pore diameter and total pore volume; however, a distinct peak around 4 nm was observed, indicating that NS promoted the formation of C–S–H gel while primarily filling pores larger than 200 nm. By 3 days, the most probable pore diameters of all samples were concentrated within 3.7–4.1 nm, and the incorporation of NCSH, NTO, and NS all effectively reduced total pore volume.

Considering the relative proportion of gel pores to capillary pores, the gel pore fraction of the C-2CSH sample increased by 292.1% and 33.6% at 12 h and 3 days, respectively, compared with the control. Meanwhile, the capillary pore fraction decreased. This result confirms that the nucleation effect of NCSH accelerated early hydration and that the generated gel products filled capillary pores. For NTO and NS samples at 12 h, the gel pore fractions increased by 118% and 92.6%, with corresponding reductions in capillary pore fractions of 9.4% and 7.3%.

3.6. Microstructural analysis

3.6.1. Matrix

Figs. 12 and 13 present the BSE images and segmented results of the cement paste matrix at 12 h and 3 days, respectively. At 12 h, the specimens containing nanomaterials exhibited substantially lower volumetric fractions of pores and unhydrated cement particles compared to the control, accompanied by a significant increase in hydration products. Among them, the C-2CSH sample displayed the fewest pores and microcracks, along with the highest proportion of hydration products, indicating that NCSH is the most effective in promoting early-age hydration and matrix densification. In comparison, the C-2NTO sample showed slightly greater structural compactness than the C-2NS sample.

At 3 days, the number of pores in all specimens further decreased, while the relative content of hydration products continued to increase. Compared with the control, the cement pastes incorporating nanomaterials still exhibited a denser microstructure. Specifically, the C-2CSH sample contained the fewest large pores and microcracks, with a limited distribution of unhydrated particles. The C-2NS sample primarily contained fine pores and only a small number of large voids, suggesting that the microstructural enhancement of NS exceeds that of NTO. These observations are consistent with the evolution trends observed in the mechanical performance of the RAC specimens.

3.6.2. Interfacial transition zone

Figs. 14–16 present the BSE images of the ITZ regions in RAC samples at 3 and 28 days, along with the relative proportions of different phases. The ITZ of RAC samples is characterized by numerous pores and microcracks; the incorporation of nanomaterials led to a reduction in both porosity and unhydrated cement content to varying degrees. Specifically, among all samples, the control exhibited the highest porosity, whereas the RAC-2.0CSH sample exhibited the lowest. A similar trend was observed for the relative content of unhydrated cement. Furthermore, the relative content of hydration products in nano-modified samples increased by 13.2–22.1% compared with the control, with RAC-2.0CSH showing the highest increase. These results confirm that NCSH has the most pronounced effect in enhancing the early microstructure of the ITZ in RAC, consistent with the observations in the cement paste matrix.

At 28 days, the pores near the recycled aggregates were further reduced, indicating that a portion of the voids had been filled by newly formed hydration products. Compared with the control, the ITZ porosity in RAC samples containing NCSH, NTO, and NS decreased by 10.1%, 9.9%, and 16.2%, respectively, while the relative content of unhydrated cement particles decreased by 8.2%, 6.3%, and 15.7%, respectively. However, the relative content of hydration products in the ITZ showed no substantial change; only the NS-containing sample exhibited a slight increase of approximately 6.6%, whereas the NCSH- and NTO-containing samples were similar to the control.

4. Discussion

The results from macroscopic mechanical properties and durability, mesoscopic ITZ analysis, and microscopic structural characterization indicate that NCSH, NTO, and NS exert distinctly stage-dependent modifying effects on RAC. These differences primarily arise from the intrinsic variations in the reactivity, nucleation capacity, and filling characteristics of the three nanomaterials. Their mechanisms of action can be classified as “nucleation-dominated,” “filling-dominated,” and “pozzolanic reaction-dominated,” as illustrated in Fig. 17.

First, the enhancement induced by NCSH is primarily governed by homogeneous nucleation. BSE imaging and TG/DTG analysis show that NCSH significantly increases the early volumetric fraction of hydration

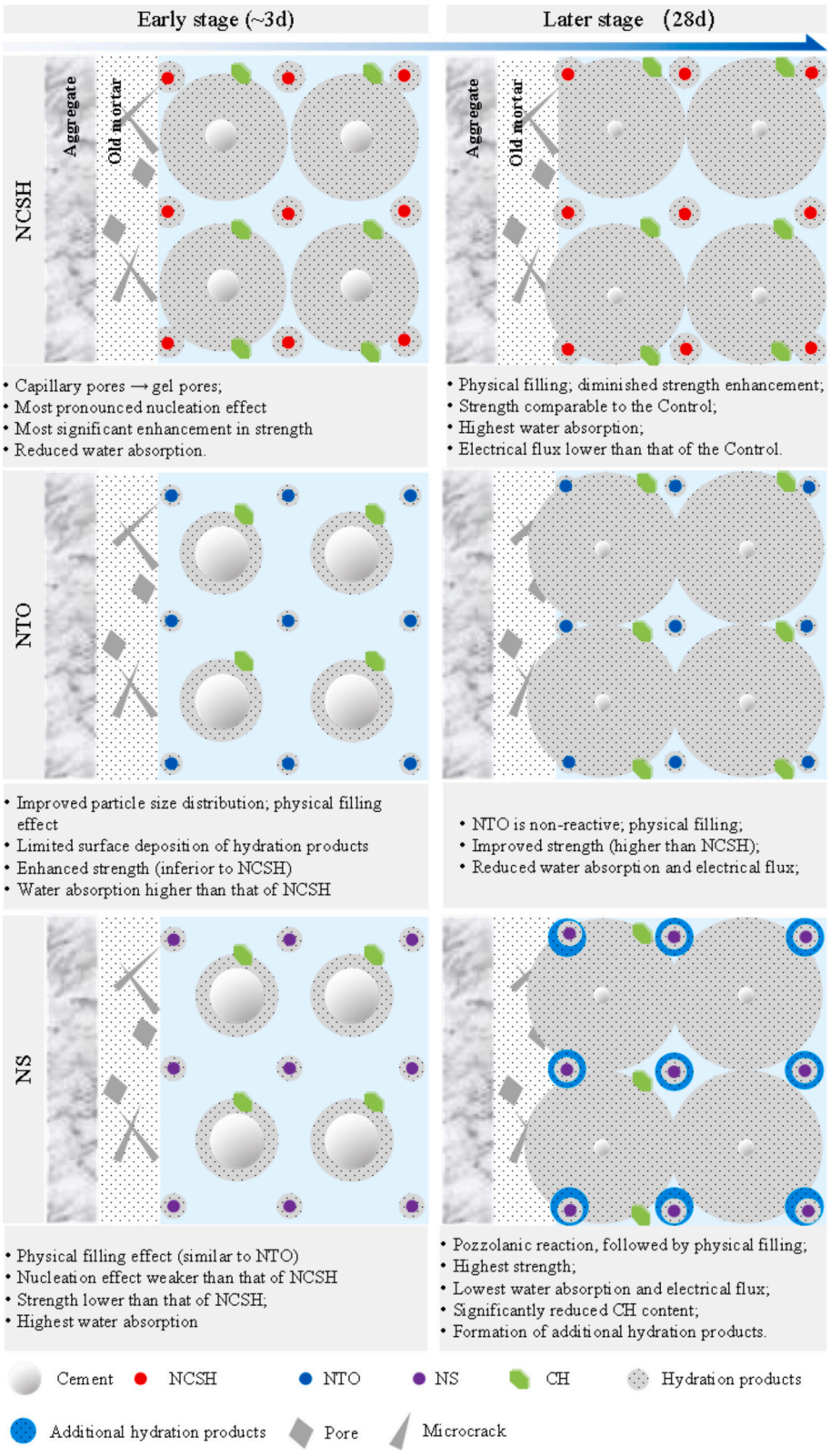

Fig. 17. Mechanistic pathways of different nanomaterials in RAC.

products (Figs. 8 and 9), while CH and CBW contents remain relatively high at all ages (Fig. 10), indicating that NCSH shortens the induction period and accelerates C-S-H formation. This is consistent with the pronounced early-age strength gain (Fig. 4) and the marked pore refinement at 12 h (Fig. 13). Water absorption results further show that the NCSH-modified samples exhibit the greatest reduction in initial absorption rate (Fig. 5), confirming its rapid suppression of early pore connectivity. This effect is also reflected in the chloride permeability results. As shown in Fig. 18, the charge passed decreases linearly with ITZ porosity ($R^2 = 0.91$), indicating that chloride transport is highly sensitive to interfacial pore continuity. In the NCSH-modified system, the rapid formation of hydrates lowers the initial ITZ porosity and

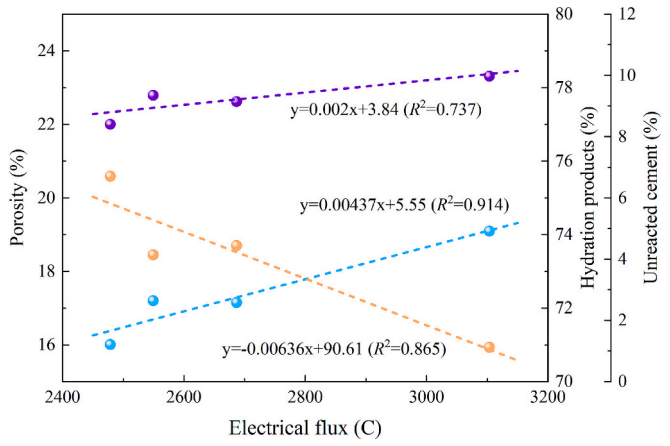

Fig. 18. The strong coupling among ITZ porosity, phase composition, and chloride ion permeability.

disrupts early connected transport paths, thereby improving early-age impermeability. However, because NCSH lacks sustained chemical reactivity, its nucleation sites are gradually covered by hydrates during hydration, which limits its contribution to later-stage structural evolution. Consequently, its improvement in 28 d chloride resistance is less pronounced than that of NS, consistent with its early-strength-dominated behavior.

Second, NTO mainly acts through physical filling, with only a weak nucleation contribution. Pore structure analysis and BSE observations indicate that NTO effectively reduces the proportion of large pores and unhydrated particles (Figs. 8 and 9) and moderately improves matrix compactness. This results in noticeable improvements in early compressive and splitting tensile strengths (Fig. 4), indicating that nanoscale filling optimizes particle packing and mitigates local defects. TG/DTG analysis shows that NTO has only a limited effect on CH content (Fig. 10), suggesting negligible participation in substantial chemical reactions. Therefore, its enhancement effect mainly relies on physical optimization of the microstructure. From the perspective of chloride transport, this filling effect mainly reduces interfacial defects and local discontinuities, thereby moderately decreasing pore connectivity in the ITZ. Because NTO does not continuously promote hydration or generate secondary gel, its contribution to long-term ITZ densification and chloride resistance remains limited. Once a relatively dense initial skeleton is formed, further performance development tends to plateau, explaining the relatively modest increase in 28 d strength and durability. Overall, NTO acts as a stable but moderate regulating material.

In contrast, NS exerts a more sustained influence on RAC. Phase analysis shows that, by 3 d, the CH content in the NS-modified samples is already lower than that in the control, indicating the onset of the pozzolanic reaction and the formation of secondary C-S-H gel (Fig. 10). Pore structure analysis further reveals a significant increase in gel pore proportion and a refinement of pore size distribution (Figs. 11–13). This ongoing secondary reaction not only consumes the relatively weak CH phase, but also continuously fills capillary pores and ITZ regions, thereby dynamically densifying the structure over time (Figs. 14–16). Fig. 18 further confirms that the decrease in ITZ porosity from 19.09% to 16.01% is accompanied by a reduction in charge passed from 3103.6 to 2478.7C, together with an increase in hydration product content from 70.93% to 75.59% and a decrease in unreacted cement from 9.97% to 8.40%. These coupled changes indicate that enhanced hydration and phase redistribution progressively reduce pore connectivity within the ITZ, thereby restricting chloride ion transport. Owing to its sustained pozzolanic reaction, NS is more effective in continuously densifying the ITZ and interrupting connected transport channels, which explains its lowest electrical flux at 28 d. Macroscopically, this is reflected in the most pronounced 28 d compressive strength gain, the lowest late-age water absorption, and the greatest reduction in electrical flux, demonstrating the superior effectiveness of NS in enhancing resistance to chloride ingress.

From an engineering perspective, the three nanomaterials should be selected according to the dominant performance requirement of RAC. NCSH is more suitable for precast or rapid-repair applications where early strength and fast setting response are critical. NTO is preferable for mixtures requiring improved structural uniformity and stable early-age enhancement with limited chemical interference. NS is the most suitable option for structures exposed to aggressive environments, where long-term impermeability and chloride resistance govern service life. Therefore, material selection should be performance-oriented rather than composition-oriented, and the distinct roles identified in this study provide a practical basis for such engineering decisions. In addition, the results suggest that a cross-timescale regulation strategy enabled by the combined use of these nanomaterials may provide a feasible route to integrate early-age nucleation, particle packing densification, and long-term pozzolanic refinement. This engineering-oriented strategy deserves further investigation for the development of high-performance RAC with balanced strength and durability.

5. Conclusions

This study compared the effects of three nanomaterials with similar particle sizes, namely NCSH, NTO, and NS, on the performance and microstructural evolution of RAC. The main conclusions are as follows:

(1) The three nanomaterials showed distinct effects on RAC performance. NCSH was the most effective in improving early-age strength, increasing the 1-day compressive and splitting tensile strengths by 56.9% and 41.9%, respectively. NS provided the greatest enhancement in 28-day strength and durability, reducing water absorption and chloride migration flux by about 20.1%. NTO improved early strength and structural uniformity, but its overall effect was comparatively moderate.

(2) All nanomaterials contributed to matrix densification by promoting hydration and refining pore structure. NCSH mainly accelerated early hydration, while NS continuously consumed CH and generated secondary C–S–H. The reduction in harmful pores and the increase in gel pores were closely associated with the improved macroscopic properties.

(3) The different performances were governed by distinct mechanisms. NCSH acted mainly through homogeneous nucleation, NTO through physical filling with limited nucleation activity, and NS through sustained pozzolanic reaction. These differences explain their respective advantages in early strength, structural uniformity, and long-term durability.

Overall, this study clarifies the distinct roles of NCSH, NTO, and NS in RAC and provides guidance for the targeted selection of nanomaterials in engineering applications.

CRediT authorship contribution statement

Jing Xu: Writing – original draft, Data curation, Conceptualization. **Peimin Zhan:** Methodology, Formal analysis, Conceptualization. **Roman Fediuk:** Project administration, Formal analysis. **Dapeng Wang:** Software. **Dongdong Wang:** Supervision. **Junqing Zuo:** Visualization, Validation. **Juan Wang:** Writing – review & editing, Funding acquisition.

Declaration of competing interest

The authors declare that they have no known competing financial interests or personal relationships that could have appeared to influence the work reported in this paper.

Acknowledgements

This work was supported by the Fundamental Research Funds for the Central Universities, CHD (300102215506).

Data availability

Data will be made available on request.

References

[1] M. Ding, S. Han, Y. Lin, Y. Wei, N. Geng, Study on the mechanical properties of recycled aggregate concrete modified by bamboo fiber-nano SiO2 synergistic effect, Constr. Build. Mater. 494 (2025) 143415.
[2] J. Yan, B. Yang, L. Feng, C. Liang, J. Xie, H. Zhang, X. Wang, F. Wang, Effect of modified jute fibre on mechanical and microstructural properties of recycled aggregate concrete, Constr. Build. Mater. 492 (2025) 143008.
[3] J. Pizoń, K. Matýsková, M. Horňáková, M. Gołaszewska, G. Kratošová, Recycled concrete paving block waste as a selected sustainable substitute for natural aggregate in cement composites, Constr. Build. Mater. 478 (2025) 141356.
[4] P. Zhan, J. Xu, J. Wang, J. Zuo, Z. He, A review of recycled aggregate concrete modified by nanosilica and graphene oxide: materials, performances and mechanism, J. Clean. Prod. 375 (2022) 134116.
[5] Z. Naseem, E. Shamsaei, K. Sagoe-Crentsil, W. Duan, Antifoaming effect of graphene oxide nanosheets in polymer-modified cement composites for enhanced microstructure and mechanical performance, Cem. Concr. Res. 158 (2022) 106843.
[6] H. Suh, D. Koo, D.-H. Son, J. Park, S. Kim, B.-I. Bae, C.-S. Choi, H. So, S. Bae, A novel strategy utilizing graphene oxide/functionalized carbon nanotube/nanosilica sheet for nanomaterial incorporation in cement paste, Cem. Concr. Compos. 157 (2025) 105918.
[7] A. Kooshkaki, H. Eskandari-Naddaf, Effect of porosity on predicting compressive and flexural strength of cement mortar containing micro and nano-silica by multi-objective ANN modeling, Constr. Build. Mater. 212 (2019) 176–191.
[8] W. Li, C. Long, V.W. Tam, C.-S. Poon, W.H. Duan, Effects of nano-particles on failure process and microstructural properties of recycled aggregate concrete, Constr. Build. Mater. 142 (2017) 42–50.
[9] T. Yang, B. Liu, L. Li, X. Gan, L. Lu, Y. Li, Agglomeration behavior of colloidal nano-silica and its effect on pore structure, mechanical properties and shrinkage of cement mortar, Constr. Build. Mater. 409 (2023) 133865.
[10] J. Jiang, H. Wang, J. Lin, Z. Liu, L. Li, Y. Li, Z. Li, L. Lu, Y. Li, Z. Lu, Accelerating mechanism of cement hydration by hydroxyl free radicals: new perspectives from photoexcited nano-TiO2, Compos. Part B Eng. 301 (2025) 112524.
[11] N. Nisar, I. Rahman, S. Paruthi, A.H. Khan, E. Sabi, A. Alyaseen, Enhancing concrete properties with nano-SiO2 and nano-TiO2: a review, J. Struct. Integr. Maint. 10 (2) (2025) 2496613.
[12] F. Wang, X. Kong, L. Jiang, D. Wang, The acceleration mechanism of nano-CSH particles on OPC hydration, Constr. Build. Mater. 249 (2020) 118734.
[13] X. Li, J. Dengler, C. Hesse, Reducing clinker factor in limestone calcined clay-slag cement using C-S-H seeding – a way towards sustainable binder, Cem. Concr. Res. 168 (2023) 107151.
[14] P. Zhan, J. Wang, W. Yu, Z. Deng, A. She, J. Zuo, W. Li, J. Xu, Insights into the hydration kinetics, microstructure and early strength of Portland cement containing synthetic C-S-H/PCE nanocomposites, Cem. Concr. Compos. 157 (2025) 105886.
[15] M.J. Garba, C. Yu, J. Liu, Q. Yuan, Y. Shalaby, X. Zhao, Y. Tian, Enhancing long-term strength of liquid-accelerated shotcrete: effect of nano-silica and synthesized nano-crystalline CSH seeds, Constr. Build. Mater. 459 (2025) 139798.
[16] T. Zhang, Y. Ogawa, K. Kawai, Mechanical properties of recycled aggregate concrete using CSH seeds and Fly ash, in: East Asia-Pacific Conference on Structural Engineering and Construction, Springer, 2024, pp. 118–125.
[17] H.M. Allujami, M. Abdulkareem, T.M. Jassam, R.A. Al-Mansob, J.L. Ng, A. Ibrahim, Nanomaterials in recycled aggregates concrete applications: mechanical properties and durability. A review, Cogent Eng. 9 (1) (2022) 2122885.
[18] L. Singh, V. Bisht, M. Aswathy, L. Chaurasia, S. Gupta, Studies on performance enhancement of recycled aggregate by incorporating bio and nano materials, Constr. Build. Mater. 181 (2018) 217–226.
[19] Y. Yue, Y. Zhou, F. Xing, G. Gong, B. Hu, M. Guo, An industrial applicable method to improve the properties of recycled aggregate concrete by incorporating nano-silica and micro-CaCO3, J. Clean. Prod. 259 (2020) 120920.
[20] L. Li, D. Xuan, S.H. Chu, J.X. Lu, C.S. Poon, Efficiency and mechanism of nano-silica pre-spraying treatment in performance enhancement of recycled aggregate concrete, Constr. Build. Mater. 301 (2021) 124093.
[21] S.A. Zaidi, M.A. Khan, T. Naqvi, A review on the properties of recycled aggregate concrete (RAC) modified with nano-silica, Mater. Today Proc. (2023).
[22] J. Bao, H. Zhang, Y. Ding, X. Chen, P. Zhang, S. Xue, L. Qin, Q. Song, Salt-frost scaling resistance characteristics of nano silica-modified recycled aggregate concrete, J. Build. Eng. 91 (2024) 109674.
[23] X. Zhang, L. Wang, Y. Shen, J. Liu, Y. Fan, Analysis of flexural fatigue damage and micro-mechanisms of nano-SiO2 modified recycled aggregate concrete, Constr. Build. Mater. 487 (2025) 142004.
[24] C. Gao, L. Huang, L. Yan, R. Jin, H. Chen, Mechanical properties of recycled aggregate concrete modified by nano-particles, Constr. Build. Mater. 241 (2020) 118030.
[25] C. Shenggang, M. Liangxiao, Y. Ruihua, W. Jieqiong, G. Junying, L. Yao, Dual-matrix enhancement mechanism of anti-corrosion performance in modified recycled aggregate concrete under chloride attack, Constr. Build. Mater. 495 (2025) 143682.
[26] P. Zhan, J. Wang, H. Zhao, W. Li, S.P. Shah, J. Xu, Impact of synthetic C-S-H seeds on early hydration and pore structure evolution of cement pastes: a study by 1H low-field NMR and path analysis, Cem. Concr. Res. 175 (2024) 107376.
[27] K. Garbev, B. Gasharova, A. Ullrich, G. Beuchle, P. Stemmermann, Assignment of SiO vibrational modes in the IR spectra of C-S-H phases based on single-crystal polarized IR and Raman spectra of 14 Å tobermorite, jennite, and jaffeite, Cem. Concr. Res. 198 (2025) 108000.
[28] H. Wong, M. Head, N. Buenfeld, Pore segmentation of cement-based materials from backscattered electron images, Cem. Concr. Res. 36 (6) (2006) 1083–1090.
[29] M. Şahmaran, V.C. Li, Influence of microcracking on water absorption and sorptivity of ECC, Mater. Struct. 42 (5) (2009) 593–603.
[30] J. Bao, L. Wang, Effect of short-term sustained uniaxial loadings on water absorption of concrete, J. Mater. Civ. Eng. 29 (3) (2017) 04016234.
[31] J. Xu, P. Zhan, W. Zhou, J. Zuo, S.P. Shah, Z. He, Design and assessment of eco-friendly ultra-high performance concrete with steel slag powder and recycled glass powder, Powder Technol. 419 (2023) 118356.
[32] P. Zhan, J. Xu, J. Wang, J. Zuo, Z. He, Structural supercapacitor electrolytes based on cementitious composites containing recycled steel slag and waste glass powders, Cem. Concr. Compos. 137 (2023) 104924.